**International Journal of Applied Mathematics**

**Volume 38 No. 12s, 2025**

ISSN: 1311-1728 (printed version); ISSN: 1314-8060 (on-line version)

# YOLO-DRIVEN GLAUCOMA SCREENING MODEL FOR PORTABLE MEDICAL SCREENING DEVICES

**Ahmed Shuqayr J Alsuayri [1, *], Ibrahim Hamad Ibrahim Aldhahi [1], Abdulkarim Saeed Alghamdi [1], Mohammed Khaled Al-Khalidi [2], Salem Awadh Saleh Alsurur [3], Adel Ghayyadh Alanazi [4], Ali Fahad Ali Alharbi [4], Mohammed Mansour Dawood [4], Naif Mohammed Almansour [5], Yahya Nafel Alanazi [5], Manar Mohammad Almutairi [6], Hussain Muharib Almarri [7], And Ali Manqal Alanazi [5]**

[1] Qassim Health cluster- Operating Administration, An Naziyah, buraydah, KSA, A 52366.

[2] Ministry of Health, Al-Sulimaniyah, Ministry of Health Headquarters (Diwan), KSA

[3] HAFERALBATIN CLUSTER, 8508 King Khalid Road, Ar Rabwah District, Hafar Al Batin, KSA, 39954

[4] Qassim Health Cluster - Buraidah Central Hospital, Al Ta'leem District, Buraidah, KSA, 52361

[5] Northern Area Armed Forces Hospital, King Khalid Military City, Hafar Al Batin, KSA, 39748

[6] Maternity and Children Hospital Buraydah, Ali Ibn Abi Talib Rd, Buraydah 52384 , KSA, 6742

[7] King Fahad Military Medical Complex, Old Abqaiq Road, Dhahran, KSA, 34313

***** Correspondence: eng.alsuayri@gmail.com

## Abstract

Glaucoma is a leading cause of irreversible blindness, and its early detection relies heavily on structural assessment of the optic nerve head, in particular the Cup-to-Disc Ratio (CDR) and Vertical Cup-to-Disc Ratio (VCDR). This work proposes a lightweight, YOLO-based computer-aided diagnosis (CAD) pipeline that automatically segments the optic disc and optic cup from colour fundus images, estimates CDR and VCDR. A dataset of 650 fundus images with disc–cup annotations was used to train a segmentation model with a 70/20/10 split for training, validation, and testing. On the validation set, the model achieved a precision of 98.98%, a recall of 99.23%, and a mean Average Precision (mAP@0.5) of 99.37%. For testing results, the model generated CDR and VCDR for each test image and mapped them to Normal, Suspect, or Glaucoma using simple rule-based thresholds, also hardware profiling showed an average end-to-end processing time of 173 ms per image and a total RAM footprint of ≈174 MB. The proposed Glaucoma Screening pipeline gives high segmentation accuracy, transparent CDR and VCDR staging, and a very small hardware requirement, which make it suitable for early glaucoma screening in portable screening devices.

**Keywords:** cup-to-disc ratio, vertical cup-to-disc ratio, YOLO, and Glaucoma

Received: August 11, 2025

Volume 38 No. 12s, 2025
ISSN: 1311-1728 (printed version); ISSN: 1314-8060 (on-line version)

## Introduction

Glaucoma is an advanced optic neuropathy; Glaucoma commonly is associated with high internal pressure of the eye. Glaucoma may lead to damage of retinal ganglion cell axons and characteristic optic-nerve head cupping [1,2]. Because early stages showing no signs of it, diagnosis is frequently delayed until essential visual loss has occurred. In 2020 about 76 million people were affected by glaucoma, and by 2024 may be raised to 112 million by 2040 [3,4]. Glaucoma disease needs for practical, scalable strategies to enable earlier screening [5 -7]. Clinical visits may be delayed due to travel constrains, financial constraints, and everyday burdens, to address these barriers, mobile medical campaigns that uses lightweight equipment can conduct initial screenings and generate initial diagnostic reports that used as reference for quick diagnostic decisions [8 - 10]. These units can operate in public, high-traffic areas as well as remote areas, while simultaneously can track disease trends over time [11 - 13]. As described in Figure 1, mobile clinical vehicles are equipped with diagnostics devices that connected to centralized Internet of Things (IoT) cloud servers. Centralized data analytics models are applied to real time data streams to monitor disease status and infection dynamics [14 - 16]. AI diagnostic models deployed in these units must be practically lightweight, memory-efficient, and fast diagnostic response time. This study introduces a lightweight Deep Learning (DL) YOLO-based glaucoma early diagnostics AI-model. Glaucoma diagnostics DL-based models has steadily moved from traditional conceptual classifiers toward clinically oriented practical pipelines. Studies report robust screening performance by training CNN models to detect optical disc cupping using real-world images alike [17 - 22].

Beyond simple binary decisions, a generalizable regression models were trained across heterogeneous datasets and emphasizes cross-dataset performance as a first-class objective [23]. A parallel line of work constrains the learning problem around clinically meaningful anatomy. Pipelines that localize the optic disc and cup and then compute VCDR or related indices improve interpretability and align predictions with clinician heuristics [24 - 26]. Such structure-aware designs can reduce black-box concerns and provide quantitative visual surrogates for triage, though they introduce the usual risk of error propagation from the segmentation/localization stage. Segmentation-centric methods push this anatomical prior further. Variants of U-Net and improved encoders are used to delineate disc/cup and sometimes nerve fiber–related layers before classification or grading, yielding measurements that map neatly to glaucomatous damage and facilitating visual verification by clinicians [27 - 28]. Grading frameworks, such as DDLS-oriented systems, shift the task from mere detection toward clinically actionable staging, tightening the link between algorithmic output and referral decisions [29]. Recent models also widen the input space and interpretability toolkit. Fusing fundus photographs with optical coherence tomography (OCT) leverages complementary surface and cross-sectional information, which is especially valuable for early disease when fundus-only cues can be subtle [30]. Attention mechanisms, transformer backbones, and Grad-CAM-style visualizations make salient regions explicit, supporting trust and rapid review without sacrificing accuracy [26, 31, 32]. Robustness under challenging phenotypes such as highly myopic eyes has been investigated to stress-test generalization beyond standard cohorts [33]. Across studies, datasets span

Received: August 11, 2025

Volume 38 No. 12s, 2025

ISSN: 1311-1728 (printed version); ISSN: 1314-8060 (on-line version)

public repositories and multi-site clinical collections, with labels ranging from binary glaucoma/suspect to multi-class staging, continuous vCDR, or clinician grades [17, 21, 22, 23, 25, 29]. Validation practices commonly include case–control splits and cross-dataset testing to gauge transportability, with metrics reported as AUC, sensitivity, specificity, and sometimes calibration analyses. Systematic and narrative reviews synthesize these trends and highlight methodological gaps limited prospective evaluations, inconsistent reporting of thresholds, and variable handling of domain shift across cameras and acquisition settings [34 - 38]. Translating these advances into portable, real-world diagnostics introduces additional constraints. Lightweight backbones and compact custom models demonstrate favorable accuracy-per-FLOP trade-offs suitable for edge devices, and several pipelines prioritize near real-time operation to match screening throughput in the field [19, 20, 21, 39]. Federated learning is emerging as a privacy-preserving strategy for multi-site updates without centralizing patient data an attractive property for population-scale screening networks [40]. Yet rigorous edge benchmarks remain scarce: few papers report model size, on-device latency, energy use, or bandwidth requirements under low-connectivity conditions. Positioned against this landscape, a YOLOv11-based tool trained on glaucoma images targets the portability gap by unifying fast localization with classification in a single, light model. Its small computational footprint and low memory use are consistent with edge deployment in mobile screening units, while attention or saliency extensions can preserve clinician interpretability in line with recent explainability-first work [19, 26, 31]. To strengthen its contribution, reporting should include cross-camera generalization, on-device latency and energy profiles, and calibrated referral thresholds, aligning with best practices surfaced by generalization-oriented and workflow-aware studies [17, 21, 23, 29]. This paper delivers a mobile glaucoma screening pipeline built on a compact YOLOv11 model that performs lesion-aware localization and risk prediction directly from fundus images, optimized for on-device inference in screening vans and low-resource settings. This paper focuses on the AI model and hardware profiling for portable glaucoma screening devices. a YOLOv11 classifier for Glaucoma disease is trained and evaluated and its computational power and runtime performance was considered [41, 42]. We report a concise hardware requirement matrix that aps desired throughput to minimal device specs, alongside exportable artifacts and inference recipes tuned for quantization and mixed precision.

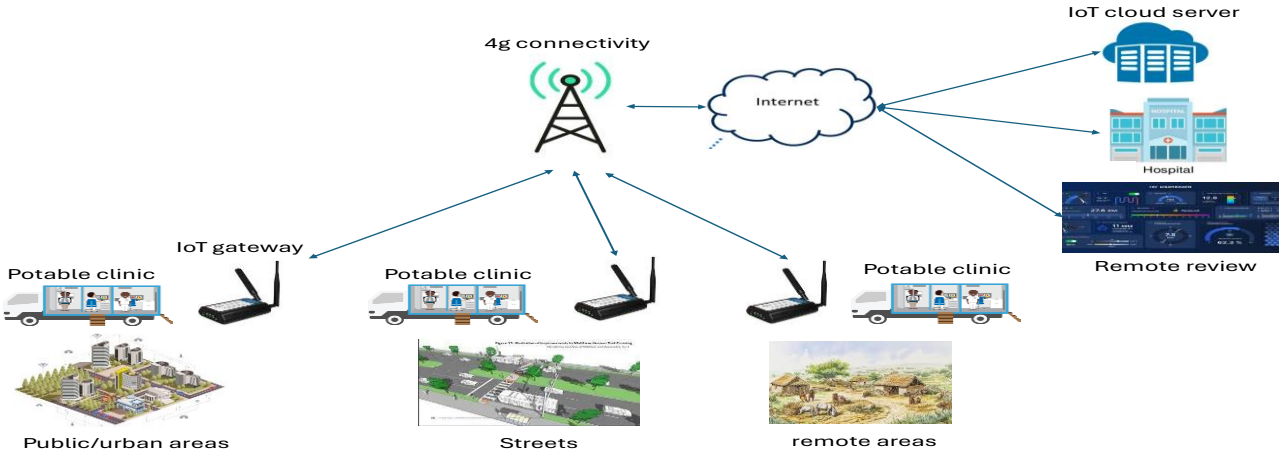


**Figure 1**. portable clinical IoT-based model

Received: August 11, 2025

International Journal of Applied Mathematics
Volume 38 No. 12s, 2025
ISSN: 1311-1728 (printed version); ISSN: 1314-8060 (on-line version)

## 2. Materials and Methods

This study follows a practical pipeline shown in Figure 2, for designing a lightweight AI model to screen for glaucoma from retinal fundus images, with a primary emphasis on runtime

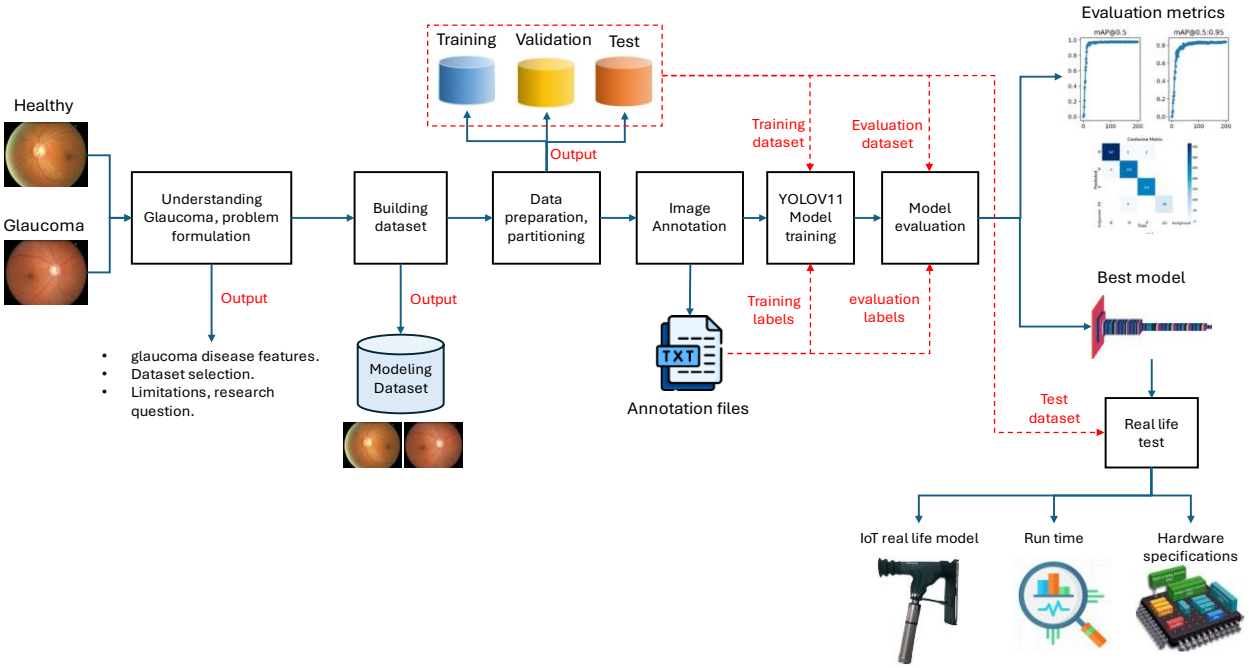


profiling and hardware requirements for edge deployment. We begin by formulating the clinical screening problem and identifying disease-relevant structural cues. We then assemble a suitable dataset and document study constraints. Images are preprocessed and split into training/validation/test sets under a reproducible protocol, followed by producing YOLO-compatible annotation files. A compact YOLOv11 model is trained and evaluated using standard metrics. The best-performing model is profiled on representative edge hardware. Finally, we derive a minimal hardware requirement matrix that maps target screening speeds to device specifications, providing actionable guidance for real-world portable deployments without building a full mobile unit.

**Figure 2**. pipeline for lightweight glaucoma screening with YOLOV11

### *2.1. Problem Formulation*

Glaucoma is failure mode affecting the optic-nerve head, Figure 3 describe the Glaucoma disease process. The upstream driver is a mismatch between aqueous humor production and outflow, which raises mechanical load at the lamina cribrosa; damage can also progress at Normal intraocular pressure (IOP) due to tissue susceptibility and vascular factors. For screening from color fundus images, the downstream, observable proxies are: vertical cup enlargement, neuroretinal rim thinning/notching, RNFL defects, disc hemorrhage, and peripapillary atrophy. Clinically, the major categories are: primary open-angle glaucoma with an open angle and

Received: August 11, 2025

Volume 38 No. 12s, 2025
ISSN: 1311-1728 (printed version); ISSN: 1314-8060 (on-line version)

increased trabecular resistance, normal-tension glaucoma (NTG) with typical damage at normal IOP, and primary angle-closure disease (PACD) where iris–trabecular contact blocks outflow [43, 44]. Secondary glaucoma arises from identifiable causes, and childhood forms stem from developmental angle anomalies or early trabecular dysfunction. Across all subtypes, the engineering target is the same: detect structural deterioration on fundus photos early and map it to a screening label (healthy / suspect / glaucoma), while accounting for confounders such as high myopia and camera/illumination variability [45, 46]. In fundus photography, glaucomatous damage presents primarily as vertical excavation of the optic nerve head, illustrated in Figure 4. Because axonal loss typically begins at the superior and inferior poles, the cup elon-

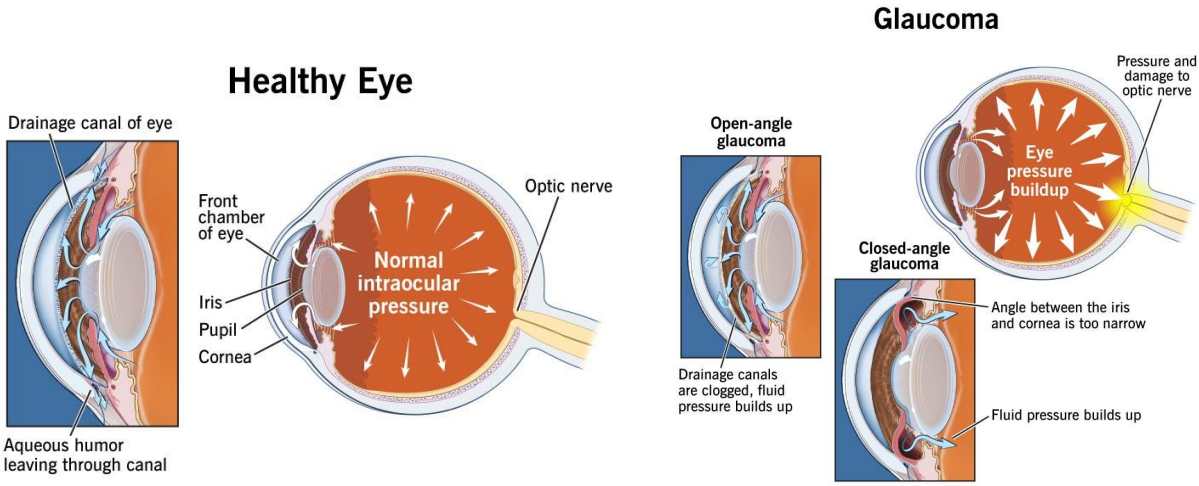


gates vertically and the neuroretinal rim thins or develops focal notches in these regions. Consequently, the VCDR is a more sensitive structural biomarker than a single horizontal or "overall"

CDR. Normal eyes commonly exhibit VCDR values around 0.3–0.5 with a continuous rim that follows the ISNT rule, whereas values ≥0.6 together with rim thinning or notching are suggestive of glaucomatous injury. CDR remains useful as a coarse descriptor but is insufficient on its own [47, 48]. Large physiologic discs can yield high CDR without disease, and early glaucoma may minimally alter the horizontal diameter while substantially increasing the vertical excavation. Robust screening therefore requires attention to the vertical geometry and to complementary cues—rim texture, wedge-shaped RNFL defects, peripapillary atrophy, vessel bayoneting, and inter-eye asymmetry. The AI diagnostics model should reliably localize disc and cup boundaries and prioritize features that capture vertical expansion and rim integrity, rather than treating CDR/VCDR as isolated scalars. This geometry-aware strategy aligns the representation learned by YOLOv11 with clinically meaningful signals while maintaining portability to real-world imaging conditions.

Received: August 11, 2025

**International Journal of Applied Mathematics**

**Volume 38 No. 12s, 2025**

ISSN: 1311-1728 (printed version); ISSN: 1314-8060 (on-line version)

**Figure 3**. health and nonhealthy glaucoma disease

**Figure 4**. Measurement of disc–cup geometry from a fundus image. The green contour delineates the optic disc and the red contour the neuroretinal cup.

Preliminary screening in portable diagnostics vehicles primarily requires a fast, robust approximation of structural risk—rather than full clinical staging—based on simple, interpretable features that can be computed in real time. Within this context, the CDR provides a practical geometric biomarker that is widely used in clinical practice as an initial indicator of glaucomatous change and can be estimated directly from fundus images. Leveraging this, we formulate the problem as designing an AI model that (i) automatically estimates the CDR from a single fundus photograph and (ii) simultaneously outputs a binary decision (glaucoma vs. non-glaucoma) suitable for use as a primary triage tool. The model must satisfy strict constraints on model size, memory footprint, and inference latency so that it can operate on low-power hardware without dependence on high-end GPUs or cloud connectivity. Accordingly, this study is guided by the following research question: "*Can a compact YOLOv12n-based model, designed to estimate the cup-to-disc ratio and perform binary glaucoma screening from fundus images, achieve clinically meaningful accuracy while meeting the computational and memory constraints required for deployment on low-cost, mobile screening hardware?*".

*2.2. Dataset preparation*

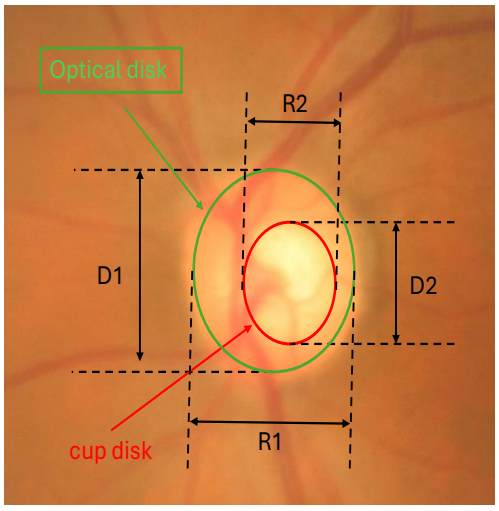


Fundus image (optical disk)

- D1: Disk height $\text{CDR} = \frac{R2}{R1}$
- D2: cup height $\text{VCDR} = \frac{D2}{D1}$

| Glaucoma stage | Glaucoma Substage | VCDR | CDR |
|---|---|---|---|
| Normal | Min | 0.3 | 0.1 |
| | Med | 0.45 | 0.26 |
| | Max | 0.6 | 0.7 |
| Moderate | Min | 0.5 | 0.2 |
| | Med | 0.64 | 0.5 |
| | Max | 0.9 | 0.7 |
| Severe | Min | 0.6 | 0.3 |
| | Med | 0.9 | 0.7 |
| | Max | 1.0 | 0.8 |

Received: August 11, 2025

**International Journal of Applied Mathematics**

**Volume 38 No. 12s, 2025**

ISSN: 1311-1728 (printed version); ISSN: 1314-8060 (on-line version)

The dataset preparation pipeline shown in Figure 5 converts heterogeneous public fundus collections into a structured, YOLOv11-seg–ready resource for optic cup–based glaucoma screening. Images are first imported from Kaggle, "*Glaucoma Fundus Imaging Datasets*" (Table 1) [49], then manually classified into *glaucoma* and *non-glaucoma* categories to ensure reliable ground-truth labels. All selected images are resized to a unified spatial resolution (e.g., 465×465) to standardize the input domain and simplify downstream training. Next, an optic disc/cup–centered region of interest is cropped from each fundus image, generating focused patches that concentrate the model's capacity on the clinically relevant structure.

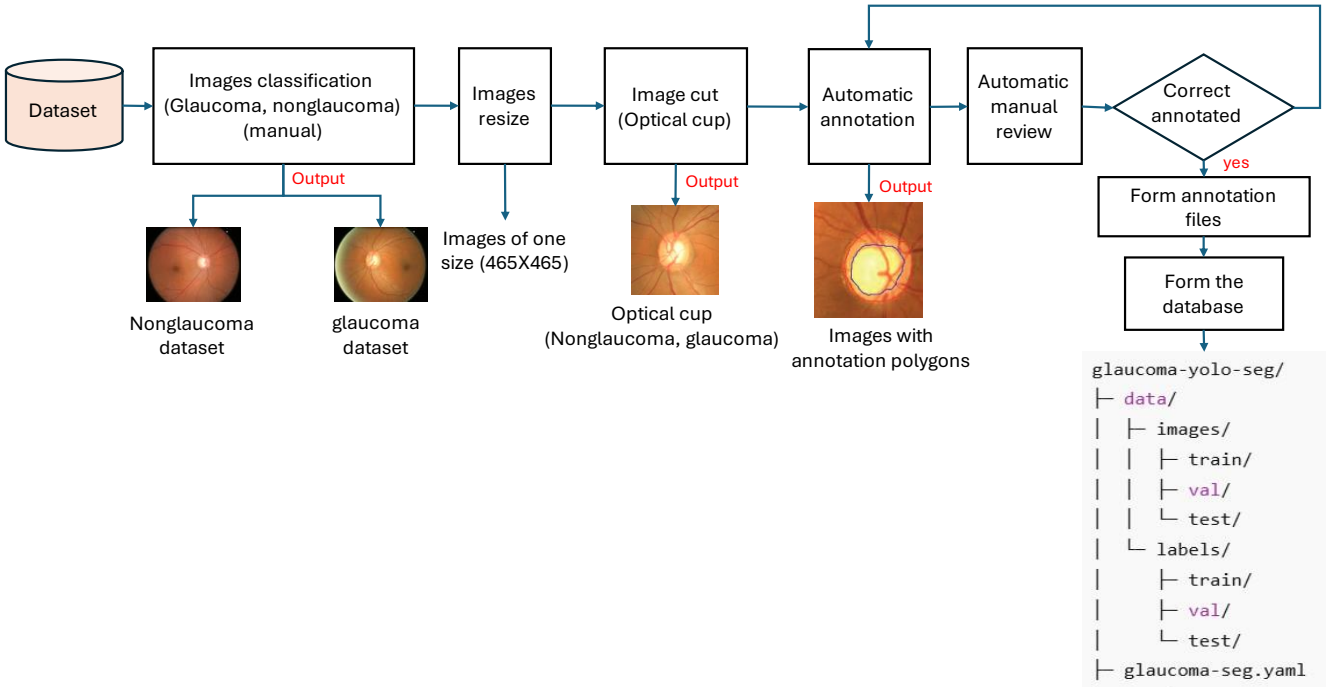


**Figure 5**. dataset formation and preprocessing

An automatic annotation step is then applied to generate initial polygon masks or contours for the optic cup; these machine-generated labels undergo targeted manual review and correction, forming a quality-controlled set of segmentation annotations[50]. Finally, correctly annotated samples are organized into a YOLO-compatible directory hierarchy with separate *images* and *labels* folders for train/validation/test splits, together with a configuration file describing class definitions and paths. This pipeline yields a compact, high-consistency dataset tailored for efficient YOLOv11-seg training and robust evaluation of cup segmentation and glaucoma classification performance.

Received: August 11, 2025

**International Journal of Applied Mathematics**

**Volume 38 No. 12s, 2025**

ISSN: 1311-1728 (printed version); ISSN: 1314-8060 (on-line version)

**Table 1**. dataset structure used for model training, evaluation, and test

| Dataset | Images | Dataset partitions | |
|---|---|---|---|
| **Glaucoma Fundus Imaging Datasets (Kaggle)** | 650 | Training | 455 |
| | | Evaluation | 130 |
| | | Test | 65 |

*2.3. Images annotation*

To construct consistent and scalable training labels, this work employs an automatic optic cup annotation pipeline tailored to YOLOv11-seg, described in Figure 6. Starting from raw color fundus images, each image is first preprocessed to enhance the visibility of the optic nerve head. The RGB image is converted to grayscale, contrast-limited adaptive histogram equalization is applied to amplify local contrast, and a Gaussian filter is used to suppress noise. On the enhanced image, high-intensity regions are extracted by thresholding around an upper percentile of the intensity distribution and refining the resulting mask using morphological opening and closing to remove isolated artifacts and fill small gaps. Contours are then computed over the cleaned binary mask. Candidate regions are filtered by minimum area, and the contour whose centroid lies closest to the image center is selected as the optic cup proxy, exploiting the typical disc–cup location in macula-centered fundus photography.

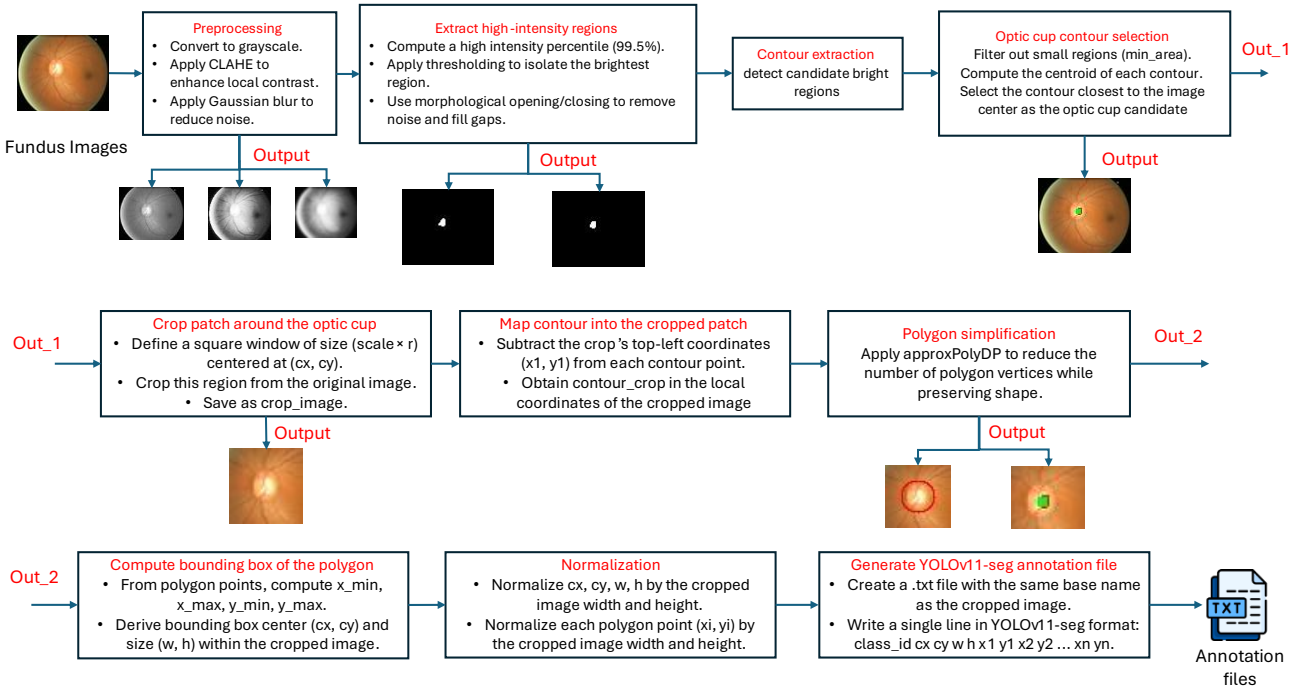


**Figure 6.** Automatic pipeline for generating YOLOv11-seg–compatible optic cup annotations from fundus photographs.

Using this selected contour, a square region of interest is cropped around the cup candidate; this patch focuses the subsequent model on the relevant structure while reducing background variability and computational cost. The original contour coordinates are re-mapped into the

Volume 38 No. 12s, 2025
ISSN: 1311-1728 (printed version); ISSN: 1314-8060 (on-line version)

coordinate system of the cropped patch, and a polygon simplification step is applied to reduce the number of vertices while preserving the essential cup shape. From the simplified polygon, the tight bounding box is computed and expressed as center coordinates and width/height within the cropped image. Figure 7 indicates visual example for one sample of dataset after applying annotation process and detect optical disc and optical cup. Both bounding-box parameters and polygon vertices are normalized by the patch dimensions to match the YOLOv11-seg specification. Finally, for each cropped image, a single annotation file is generated containing the class identifier and the normalized bounding box and polygon coordinates in the required format.

For each cropped optic disc–centered fundus image, annotations were generated using the YOLOv11-seg format to jointly encode class label, bounding box, and segmentation mask of the optic cup. Each object instance is represented by a single line of space-separated values described in Table 2. The class_id denotes the glaucoma status of the eye associated with the annotated optic cup and follows a fixed mapping: 0 for non-glaucoma and 1 for glaucoma. The terms cx and cy represent the normalized coordinates of the bounding box center, while w and h denote the normalized width and height of the bounding box enclosing the cup; all four values are scaled to the range $[0,1]$ relative to the dimensions of the cropped image. The sequence $(x_1, y_1)$ encodes the segmentation mask as a polygonal contour tightly outlining the optic cup region. Each polygon vertex is expressed in normalized image coordinates, where $x_i \in [0,1]$ and $y_i \in [0,1]$ correspond to the horizontal and vertical positions relative to the cropped image width and height, respectively.

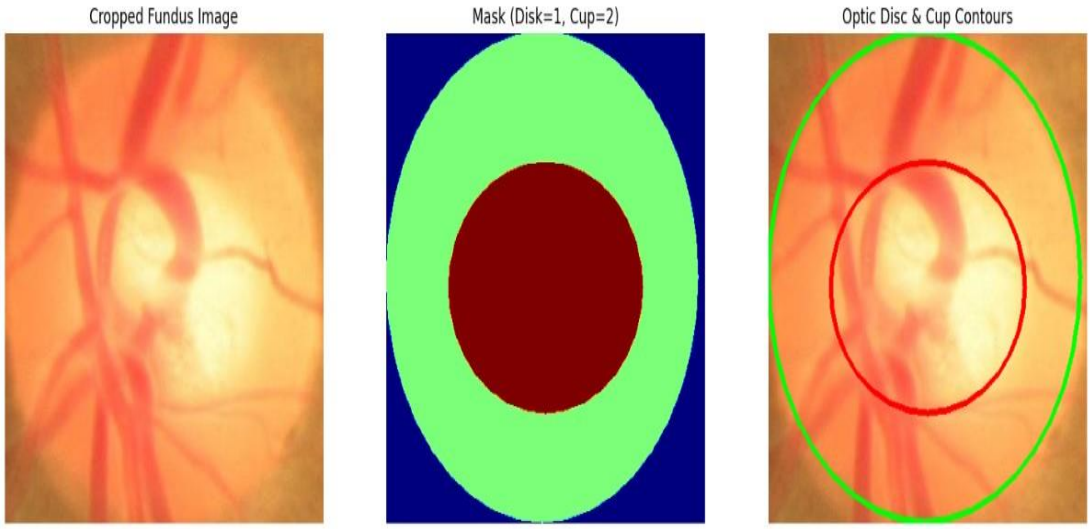


**Figure 7**. visual example for image preparation, and annotation

Received: August 11, 2025

**International Journal of Applied Mathematics**

**Volume 38 No. 12s, 2025**

ISSN: 1311-1728 (printed version); ISSN: 1314-8060 (on-line version)

**Table 2**. the YOLOV12-Seg annotation file content description

| Field | Description | Value Type | Range / Allowed Values |
|---|---|---|---|
| **class_id** | Integer label of the object/mask | Integer | 0 = optical disk, 1 = optical cup |
| **cx** | x-coordinate of the bounding box center | Float (normalized) | (0 = left edge, 1 = right edge) |
| **cy** | y-coordinate of the bounding box center | Float (normalized) | (0 = top edge, 1 = bottom edge) |
| **w** | width of the bounding box enclosing the polygon. | Float (normalized) | (must be > 0; typically, < 1). |
| **h** | height of the bounding box enclosing the polygon. | Float (normalized) | (must be > 0; typically, < 1). |
| **x1, y1** | coordinates of the first polygon vertex outlining the optic cup region. | Floats (normalized) | Each xi in [0.0, 1.0]<br>each yi in [0.0, 1.0] |

*2.4. Model training, evaluation, and testing*

The overall training and deployment pipeline of the proposed glaucoma-detection system is summarized in Figure 8. First, the annotated fundus images are split into three subsets: a training dataset with corresponding YOLO-formatted TXT labels, an evaluation dataset with its labels, and an independent test dataset. The training images and labels are fed into the YOLO-V11 network, and the model is iteratively optimized by adjusting key hyperparameters such as learning rate, batch size, and number of epochs. After each training cycle, the current weights are re-evaluated on the evaluation dataset to compute quantitative performance indicators, including confusion matrix, precision–recall curve, loss curves, and mAP scores. These metrics are inspected to decide whether the model satisfies the predefined acceptance criteria; otherwise, the training parameters are tuned and the loop is repeated until an accepted model is obtained. Once the model is accepted, the best-performing weights are frozen and used for inference on the test dataset, where the network localizes the optic disc and optic cup for each

Received: August 11, 2025

Volume 38 No. 12s, 2025

ISSN: 1311-1728 (printed version); ISSN: 1314-8060 (on-line version)

image. Based on these detections, the system calculates clinically relevant structural biomarkers, CDR and VCDR. Finally, a threshold analysis is applied to these indices to categorize each case into one of three clinically meaningful classes Normal, Suspect, or Glaucoma. As part of the system evaluation, we conduct a hardware performance assessment to determine the specifications required for deploying the trained glaucoma-detection model in mobile or vehicle-based screening units. The analysis focuses on estimating the essential computational parameters, including the average inference time per image, CPU utilization, RAM consumption during model execution, and the impact of input resolution on processing speed. These measurements allow us to identify the minimum hardware capabilities needed to ensure stable and efficient operation of the model in portable, GPU-free environments.

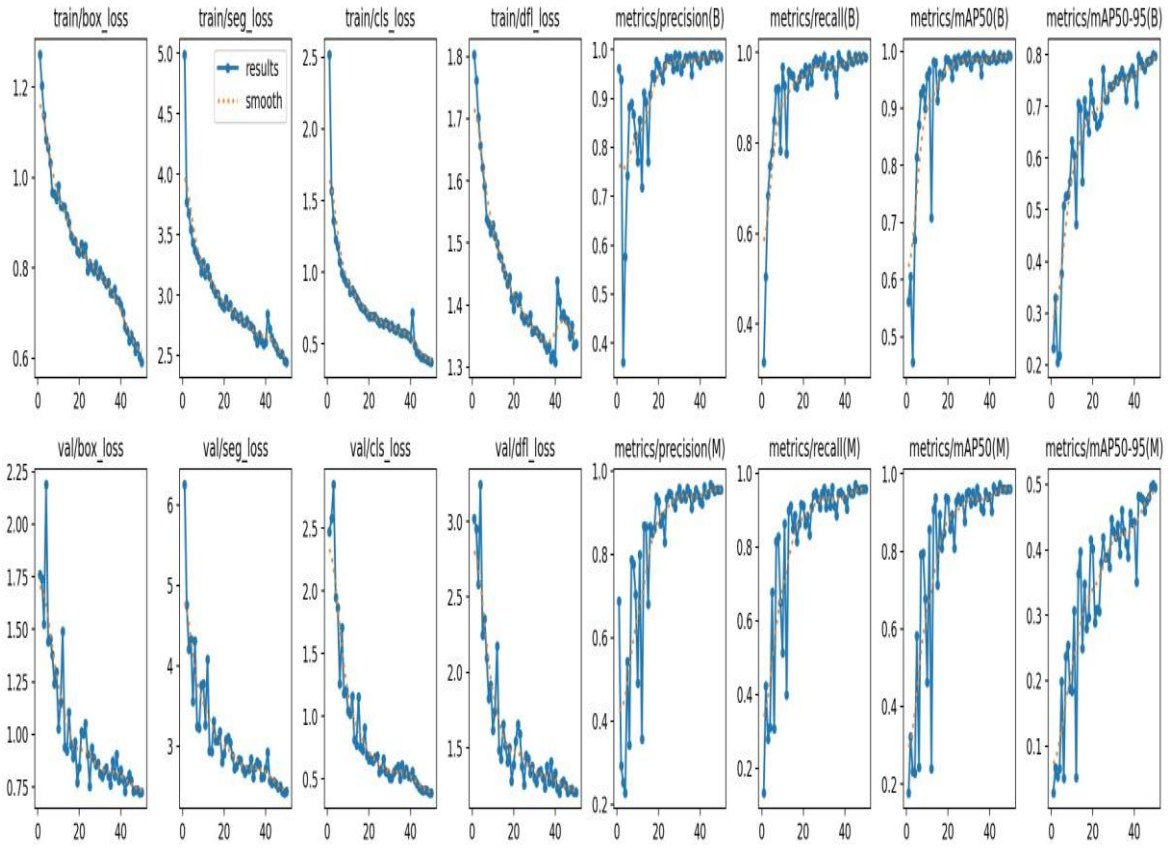


**Figure 8**. YOLOV11 training and evaluation

## 3. Results

### *3.1. Training and evaluation results*

The proposed YOLO-based model was trained using a 70/20/10 split for training, validation, and testing, respectively. After convergence, the final model achieved very strong performance on the detection and segmentation of the optic disc and optic cup. As described in Figure 9, for the bounding-box branch, the model reached a precision of about 98.98% and a recall of

Received: August 11, 2025

Volume 38 No. 12s, 2025

ISSN: 1311-1728 (printed version); ISSN: 1314-8060 (on-line version)

99.23%, with an mAP@0.5 of 99.37% and an mAP@0.5–0.95 of approximately 80%. For the segmentation (mask) branch, the precision and recall were 95.52% and 95.77%, respectively, with an mAP@0.5 close to 96% and an mAP@0.5–0.95 of about 50%. These values indicate that the model is highly reliable in localizing both the optic disc and the optic cup, which is essential for accurately computing the CDR and VCDR ratios. The confidence-based curves

**Figure 9**. segmentation and bounding box performance analysis

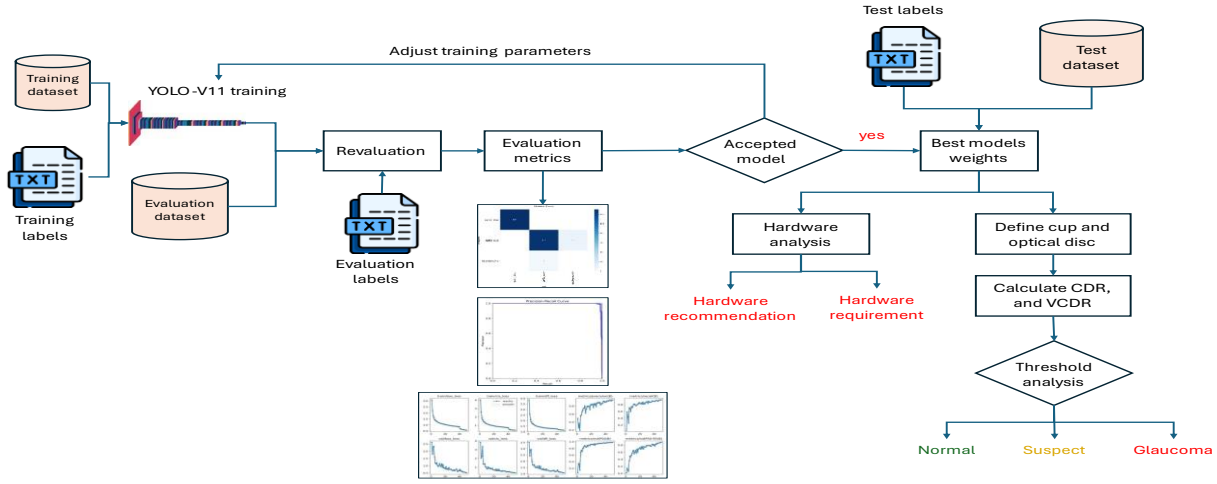


presented in Figure 10 provide further insight into the behavior of the proposed model. The F1–confidence curve shows that the combined classes (optic disc and optic cup) achieve a maximum F1-score of approximately 0.99 at a confidence threshold of about 0.474, indicating an excellent balance between precision and recall at this operating point. The precision–confidence curve remains very close to 1.0 over a wide range of confidence values for both structures, with the “all classes” curve reaching a precision of 1.00 at a confidence of 0.928. The precision–recall (PR) curve further confirms the robustness of the detector, where the area under the curve corresponds to an mAP@0.5 of 0.995 for the optic disc, 0.992 for the optic cup, and 0.994 when averaged over all classes. Finally, the recall–confidence curve demonstrates that recall remains close to 1.0 for low and moderate confidence thresholds and only starts to decline at very high confidence levels. Together, these curves corroborate the results in Table 3 and verify that the chosen confidence threshold yields a stable operating region in which both optic disc and optic cup are detected with near-perfect precision and recall, thereby supporting reliable computation of the CDR and VCDR ratios.

In order to further analyze the behavior of the proposed model, the normalized confusion matrix for the validation set is presented in Figure 11. the diagonal elements are almost equal to 1.00 for all classes, indicating that the vast majority of samples are correctly classified. In particular, the optic disc class is recognized with a normalized accuracy of 1.00, with no noticeable

Received: August 11, 2025

**Volume 38 No. 12s, 2025**

ISSN: 1311-1728 (printed version); ISSN: 1314-8060 (on-line version)

confusion with either the optic cup or the background. The optic cup class is also predicted very reliably, with approximately 0.98 of the samples correctly assigned to the optic cup and only about 0.02 being misclassified as background. The background region itself is also classified with a normalized value close to 1.00, and the off-diagonal entries remain close to zero. This pattern in the confusion matrix confirms that there is negligible confusion between the optic disc and optic cup classes and that the network is highly capable of separating anatomical structures from the background, which is crucial for obtaining precise CDR and VCDR measurements

**Figure 10.** F1–Confidence, Precision–Confidence, Precision–Recall, and Recall–Confidence curves for the proposed YOLO-based optic disc and optic cup detector.

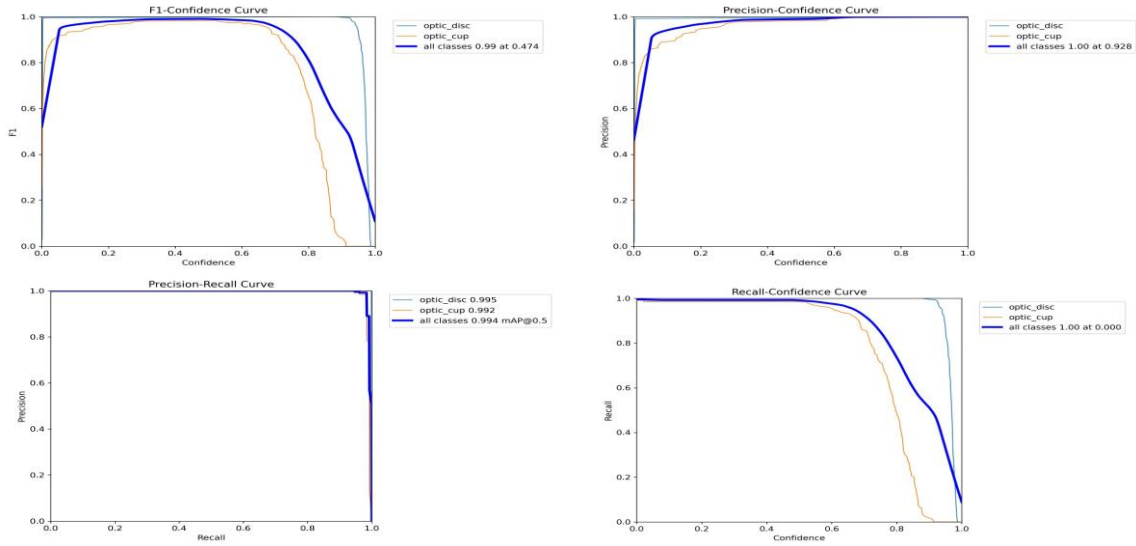


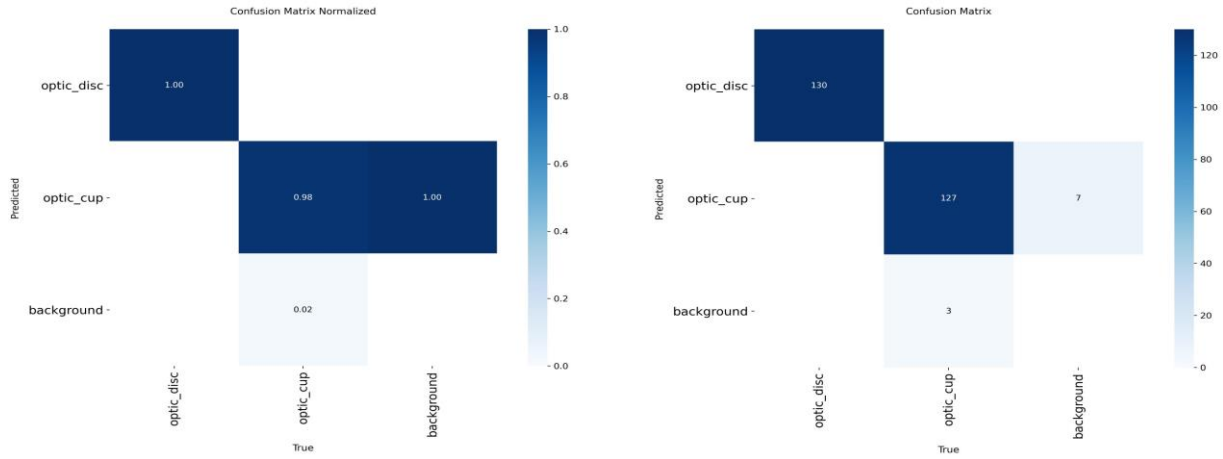


**Figure 11**. Confusion matrices for the proposed YOLO-based optic disc and optic cup

Received: August 11, 2025

**International Journal of Applied Mathematics**

**Volume 38 No. 12s, 2025**

ISSN: 1311-1728 (printed version); ISSN: 1314-8060 (on-line version)

**Table 3**. description of the segmentation and bounding box performance analysis

| Metric | Optic Disc | Optic Cup | All Classes (Mean) |
|---|---|---|---|
| **Precision (%)** | 99.5 | 99.2 | 99.4 |
| **Recall (%)** | 99.6 | 99.0 | 99.3 |
| **F1-score (at optimal confidence)** | 0.99 | 0.97 | 0.99 |
| **mAP@0.5 (%)** | 99.5 | 99.2 | 99.4 |
| **PR Curve AUC** | ≈1.00 | ≈0.99 | ≈1.00 |

*3.2. Model testing results*

For the final evaluation, the proposed pipeline was tested on an independent subset of 65 fundus images out of the 650-image dataset (10%), which was not used during training or validation. For each test image, the YOLO-based model was first applied to segment the optic disc and optic cup and to derive the corresponding geometric measurements. The vertical disc height $D1$, vertical cup height $D2$, disc radius $R1$, and cup radius $R2$ were then used to compute the CDR and the VCDR for every eye. These automatically estimated indices were subsequently mapped to glaucoma severity levels using the threshold ranges summarized in Figure 4, where CDR and VCDR intervals are defined for Normal, Moderate, and Severe stages and their Min/Med/Max substages. In this way, the model output for each of the 65 test images consists of a pair of quantitative structural biomarkers (CDR, VCDR) and a corresponding categorical decision (Normal, Suspect/Moderate, or Severe) that is fully consistent with the clinical staging rules encoded in the table. To further illustrate how the proposed system would behave in a practical deployment scenario, the entire test set of 65 eyes was processed and visualized as a single collage, as shown in Figure 12. For each fundus image, the model automatically segmented the optic disc (green contour) and optic cup (red contour), computed the corresponding CDR and VCDR values, and assigned a glaucoma stage (Normal, Suspect, or Glaucoma) according to the rule-based thresholds. The figure demonstrates that, for the vast majority of cases, the contours closely follow the true anatomical boundaries and the reported ratios fall within clinically plausible ranges, confirming that the network can provide stable, patient-level outputs that are directly usable in practice. One test image, is severely degraded and does not contain sufficient information to reliably delineate the disc and cup. For this eye, the system fails to produce meaningful measurements and the stage is marked as *Unknown*. This single ambiguous case is intentionally retained in the figure to emphasize that the proposed pipeline not only performs well on typical images, but also explicitly exposes its

Volume 38 No. 12s, 2025
ISSN: 1311-1728 (printed version); ISSN: 1314-8060 (on-line version)

uncertainty when the image quality is too poor, thereby encouraging the integration of basic quality-control checks in real screening workflows.

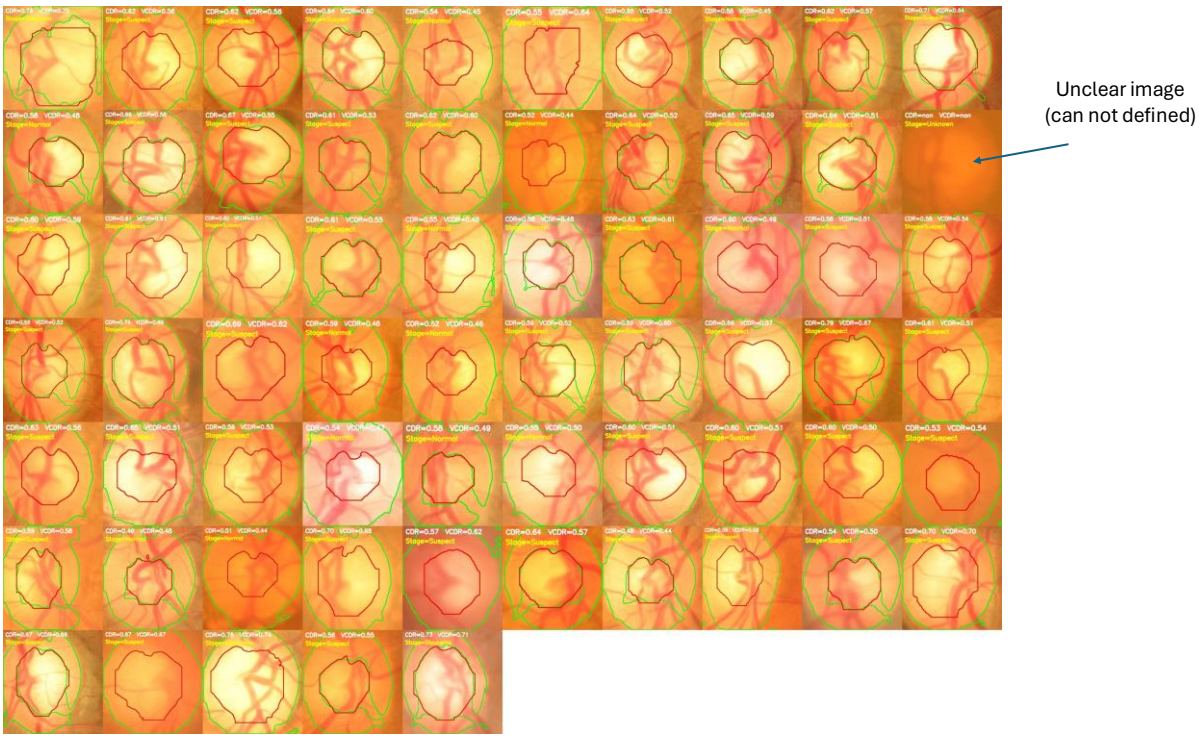


**Figure 12**. Collage of the 65 test fundus images with the model's disc (green) and cup (red) segmentations, calculated CDR/VCDR values, and assigned glaucoma stages.

*3.3. Hardware test results*

To assess the feasibility of deploying the proposed glaucoma-screening pipeline in mobile or low-resource clinical units, the full end-to-end system was profiled on a CPU-only environment using the 65-image test set. The results, summarized in Table 4, demonstrate that the model is computationally lightweight and capable of real-time performance without requiring a GPU. The average processing time per image including image loading, disc/cup segmentation, CDR/VCDR computation, and rule-based staging was 173 ms, with a minimum of 160.81 ms and a maximum of 350.32 ms, corresponding to a throughput of approximately 5.7 images per second. This level of latency is more than sufficient for real-time screening in mobile ophthalmic vehicles, where patient flow is typically far slower than the model's peak processing rate. In terms of memory usage, the baseline RAM consumption before model loading was 111.75 MB, increasing to 173.71 MB after running the full pipeline. This indicates a modest overhead of roughly 62 MB for model weights, runtime buffers, and intermediate computations. The average extra RAM consumed during the processing of each image was only 0.95 MB, with short transient peaks up to 50.64 MB, which remain well within the capabilities of lightweight embedded PCs commonly used in mobile screening units. The model itself is compact, with a file size of only 5.73 MB and approximately 2.84 million parameters,

Received: August 11, 2025

Volume 38 No. 12s, 2025
ISSN: 1311-1728 (printed version); ISSN: 1314-8060 (on-line version)

corresponding to an estimated parameter memory footprint of 10.85 MB. These values confirm that the system imposes minimal hardware requirements and can be integrated into portable devices or vehicle-mounted workstations without specialized hardware acceleration.

**Table 4**. Hardware performance metrics of the proposed pipeline

| Metric | Value |
|---|---|
| **Average processing time per image** | 173.00 ms |
| **Min / Max processing time** | 160.81 – 350.32 ms |
| **Processing throughput** | 5.74 images/s |
| **Baseline RAM (before pipeline)** | 111.75 MB |
| **Total RAM at end of pipeline** | 173.71 MB |
| **Approx. additional RAM required** | ~62 MB |
| **Average extra RAM per image** | 0.95 MB |
| **Min / Max extra RAM (transient)** | 0.22 – 50.64 MB |
| **Model file size** | 5.73 MB |
| **Number of parameters** | 2,842,998 |
| **Estimated parameter memory** | 10.85 MB |

## 4. Discussion

This study presented a pipeline for automatic glaucoma screening based on CDR and VCDR analysis. By using a compact YOLOV12-Seg DL model, the Glaucoma diagnostic system can measure the CDR and VCDR ratios and convert them into useful information for Glaucoma diagnostics. The mAP segmentation performance of the trained model was close to 1.0 and confusion matrices results showed almost purely diagonal structure. A key novelty of our approach is that glaucoma diagnostic stage is determined from the CDR and VCDR ratios that predicted by the trained model and explicit rule-based thresholds are used. The mobile clinical units can inspect the fundus image, the disc–cup, the CDR and VCDR ratios, and the assigned prediction initial diagnostic stage (Normal, Suspect, or Glaucoma). The hardware testing results showed that the complete diagnostic pipeline can be used in real-time on a CPU-based platform or any embedded computers, where the fundus image processing approximately run in 0.17 s with a total memory below 200 MB and a model size of only 5.73 MB. These hardware characteristics make the developed model is suitable for integration into mobile clinical diagnostics units, and portable fundus cameras. Future work will focus on coupling the proposed vision module with IoT-enabled acquisition hardware and electronic health record systems would enable large-scale, continuous population screening for glaucoma, helping to detect the disease earlier and reduce preventable vision loss.

Received: August 11, 2025

Volume 38 No. 12s, 2025

ISSN: 1311-1728 (printed version); ISSN: 1314-8060 (on-line version)

## 6. Patents

No patents resulting from the work reported in this manuscript.

**Supplementary Materials:** Supporting information are:

**Dataset**: original dataset download links are includes within references [49], cropped images are included within the supplementary material.

**Model Training and evaluation codes**: model trained and evaluated on Kaggle platform, included within submission

**Model testing codes**: included within submission

**Trained model results (best model, evaluations)**: included with submission

**Figures**: are included within submission.

**Author Contributions:** Conceptualization, and methodology A.SH.A, A.M.AL, and A.Gh.A;, A.SH.A. S.A.S.AL. and N.M.A.; software, validation, and formal analysis A.M.AL, Y.N.A, H.M.AL, and M.M.D; investigation, resources, and data curation M.M.A, I.H.I, and A.S.AL; writing—original draft preparation, writing—review and editing, M.Kh.Al, A.SH.A, and A.M.AL, visualization, A.Gh.A, Y.N.A, A.SH.A; supervision, project administration, A.SH.A. All authors have read and agreed to the published version of the manuscript.".

**Funding:** "This research received no external funding".

**Institutional Review Board Statement:** "Not applicable"

**Informed Consent Statement:** "Not applicable."

**Data Availability Statement:** data are available at reference [49].

**Acknowledgments:** The authors employed ChatGPT (OpenAI) for language polishing, drafting alternative figure captions, and paraphrasing selected passages (I. INTRODUCTION, literature part; II. RESULTS, Hardware test results part). All AI-assisted text was reviewed and approved by the authors, who take full responsibility for the work. Analytical methods, experiments, and results were conceived and executed by the authors without AI-generated content. References were prepared using Mendeley.

**Conflicts of Interest:** "The authors declare no conflicts of interest."

## Abbreviations

The following abbreviations are used in this manuscript:

| | |
|---|---|
| CDR | Cup-to-Disc Ratio |
| VCDR | Vertical Cup-to-Disc Ratio |
| CAD | Computer-Aided Diagnosis |
| OCT | Optical Coherence Tomography |
| IOP | Normal Intraocular Pressure |

Volume 38 No. 12s, 2025
ISSN: 1311-1728 (printed version); ISSN: 1314-8060 (on-line version)

NTG Normal-Tension Glaucoma

## References

[1] J. J. García-Medina and M. D. Pinazo-Durán, "Updates in Clinical and Translational Glaucoma Research," *Journal of Clinical Medicine 2022, Vol. 11, Page 221*, vol. 11, no. 1, p. 221, Dec. 2021, doi: 10.3390/JCM11010221.

[2] R. K. Goit, "Exploring Glaucoma: From Pathogenesis to Emerging Diagnostic and Management Strategies," *J Ophthalmol*, vol. 2025, no. 1, p. 8476785, Jan. 2025, doi: 10.1155/JOPH/8476785.

[3] Y. C. Tham, X. Li, T. Y. Wong, H. A. Quigley, T. Aung, and C. Y. Cheng, "Global prevalence of glaucoma and projections of glaucoma burden through 2040: a systematic review and meta-analysis," *Ophthalmology*, vol. 121, no. 11, pp. 2081–90, Nov. 2014, doi: 10.1016/j.ophtha.2014.05.013.

[4] M. H. Shahriari, F. Asadi, H. Moghaddasi, A. Roshanpour, F. Sharifipour, and Z. Khorrami, "Applications of machine learning in glaucoma diagnosis based on tabular data: a systematic review," *BMC Biomedical Engineering 2025 7:1*, vol. 7, no. 1, pp. 9-, Aug. 2025, doi: 10.1186/S42490-025-00095-3.

[5] D. M. H. Nguyen *et al.*, "Deep Learning for Ophthalmology: The State-of-the-Art and Future Trends," Jan. 2025, Accessed: Nov. 15, 2025. [Online]. Available: https://arxiv.org/pdf/2501.04073

[6] J. Zhang, B. Tian, M. Tian, X. Si, J. Li, and T. Fan, "A scoping review of advancements in machine learning for glaucoma: current trends and future direction," *Front Med (Lausanne)*, vol. 12, p. 1573329, Apr. 2025, doi: 10.3389/FMED.2025.1573329/BIBTEX.

[7] A. Mokhtari, B. M. Maris, and P. Fiorini, "A Survey on Optical Coherence Tomography—Technology and Application," *Bioengineering 2025, Vol. 12, Page 65*, vol. 12, no. 1, p. 65, Jan. 2025, doi: 10.3390/BIOENGINEERING12010065.

[8] S. Hu *et al.*, "Digital health: current applications, challenges, and future directions for enhancing healthcare quality and safety," *Front Public Health*, vol. 13, p. 1646802, Sep. 2025, doi: 10.3389/FPUBH.2025.1646802/FULL.

[9] N. Kaur, A. Mittal, and A. Gupta, "Neonatal Jaundice Detection: A Comprehensive Survey from Manual to Computer-Aided Methods," *Journal of Bionic Engineering 2025*, pp. 1–31, Oct. 2025, doi: 10.1007/S42235-025-00789-3.

Received: August 11, 2025 

**Volume 38 No. 12s, 2025**

ISSN: 1311-1728 (printed version); ISSN: 1314-8060 (on-line version)

[10] S. Mahadik, P. Sen, and E. J. Shah, "Harnessing digital health technologies and real-world evidence to enhance clinical research and patient outcomes," *Digit Health*, vol. 11, May 2025, doi: 10.1177/20552076251362097.

[11] B. Al Knawy, "Global Data and Digital Public Health Leadership for Current and Future Pandemic Responses," *Front Digit Health*, vol. 3, p. 632568, Jan. 2021, doi: 10.3389/FDGTH.2021.632568/BIBTEX.

[12] H. Schlieter, K. Gand, L. A. Marsch, W. S. Chan, and T. Kowatsch, "Editorial: Scaling-up health-IT—sustainable digital health implementation and diffusion," *Front Digit Health*, vol. 6, p. 1296495, Apr. 2024, doi: 10.3389/FDGTH.2024.1296495/BIBTEX.

[13] C. Ndayishimiye, H. Lopes, and J. Middleton, "A systematic scoping review of digital health technologies during COVID-19: a new normal in primary health care delivery," *Health and Technology 2023 13:2*, vol. 13, no. 2, pp. 273–284, Jan. 2023, doi: 10.1007/S12553-023-00725-7.

[14] R. Kalia, M. Aledhari, M. Rahouti, and A. Chehri, "DeepRet: A Portable and Multi-modal AI System for Enhancing Glaucoma Diagnosis in Resource-Limited Settings," *Procedia Comput Sci*, vol. 270, pp. 5922–5931, Jan. 2025, doi: 10.1016/J.PROCS.2025.10.061.

[15] K. G. Devi, A. Balachandran, B. Logesh, B. Sudha, and K. Yogeshwaran, "Machine Learning based Glaucoma Detection using Electroretinography (ERG) Signals for Early Diagnosis and Monitoring," *Proceedings of 7th International Conference on Inventive Material Science and Applications, ICIMA 2025*, pp. 436–441, 2025, doi: 10.1109/ICIMA64861.2025.11073871.

[16] P. Wankhede, T. Bhusari, V. Tammewar, R. Agrawal, C. Dhule, and N. C. Morris, "IoT & AI-ML Based Portable Non-Contact Retinal Imaging for Glaucoma and Eye Disease Monitoring at Home," *International Conference on Emerging Trends in Engineering and Technology, ICETET*, 2025, doi: 10.1109/ICETETSIP64213.2025.11156562.

[17] K. H. Hung *et al.*, "Application of a deep learning system in glaucoma screening and further classification with colour fundus photographs: a case control study," *BMC Ophthalmol*, vol. 22, no. 1, Dec. 2022, doi: 10.1186/s12886-022-02730-2.

[18] S. Joshi, B. Partibane, W. A. Hatamleh, H. Tarazi, C. S. Yadav, and D. Krah, "Glaucoma Detection Using Image Processing and Supervised Learning for Classification," *J Healthc Eng*, vol. 2022, 2022, doi: 10.1155/2022/2988262.

Received: August 11, 2025 

**Volume 38 No. 12s, 2025**

ISSN: 1311-1728 (printed version); ISSN: 1314-8060 (on-line version)

[19] S. Das, M. Mishra, and S. Majumder, "Identification of Glaucoma from Retinal Fundus Images using Deep Learning Model, MobileNet," *ECTI Transactions on Computer and Information Technology*, vol. 18, no. 3, pp. 371–380, Jul. 2024, doi: 10.37936/ecti-cit.2024183.256182.

[20] G. D'Souza, P. C. Siddalingaswamy, and M. A. Pandya, "AlterNet-K: a small and compact model for the detection of glaucoma," *Biomed Eng Lett*, vol. 14, no. 1, pp. 23–33, Jan. 2024, doi: 10.1007/s13534-023-00307-6.

[21] S. Saha, J. Vignarajan, and S. Frost, "A fast and fully automated system for glaucoma detection using color fundus photographs," *Sci Rep*, vol. 13, no. 1, Dec. 2023, doi: 10.1038/s41598-023-44473-0.

[22] walaa hassan Hagar, N. Eladawi, dalia sabry, and H. Salaheldine, "Enhancing Glaucoma Detection Using Convolutional Neural Networks: A Comparative Study of Multi-Class and Binary Classification Approaches," *Alfarama Journal of Basic & Applied Sciences*, vol. 0, no. 0, pp. 0–0, Nov. 2024, doi: 10.21608/ajbas.2024.324901.1232.

[23] R. Hemelings *et al.*, "A generalizable deep learning regression model for automated glaucoma screening from fundus images," *NPJ Digit Med*, vol. 6, no. 1, Dec. 2023, doi: 10.1038/s41746-023-00857-0.

[24] M. Nawaz *et al.*, "An Efficient Deep Learning Approach to Automatic Glaucoma Detection Using Optic Disc and Optic Cup Localization," *Sensors*, vol. 22, no. 2, Jan. 2022, doi: 10.3390/s22020434.

[25] X. R. Gao, F. Wu, P. T. Yuhas, R. K. Rasel, and M. Chiariglione, "Automated vertical cup-to-disc ratio determination from fundus images for glaucoma detection," *Sci Rep*, vol. 14, no. 1, Dec. 2024, doi: 10.1038/s41598-024-55056-y.

[26] H. Alasmari, G. Amoudi, and H. Alghamdi, "Explainable Transformer-Based Framework for Glaucoma Detection from Fundus Images Using Multi-Backbone Segmentation and vCDR-Based Classification," *Diagnostics*, vol. 15, no. 18, Sep. 2025, doi: 10.3390/diagnostics15182301.

[27] R. Kashyap, R. Nair, S. M. P. Gangadharan, M. Botto-Tobar, S. Farooq, and A. Rizwan, "Glaucoma Detection and Classification Using Improved U-Net Deep Learning Model," *Healthcare (Switzerland)*, vol. 10, no. 12, Dec. 2022, doi: 10.3390/healthcare10122497.

[28] M. B. Sudhan *et al.*, "Segmentation and Classification of Glaucoma Using U-Net with Deep Learning Model," *J Healthc Eng*, vol. 2022, 2022, doi: 10.1155/2022/1601354.

Received: August 11, 2025 

Volume 38 No. 12s, 2025
ISSN: 1311-1728 (printed version); ISSN: 1314-8060 (on-line version)

[29] H. A. Rasheed *et al.*, "DDLSNet: A Novel Deep Learning-Based System for Grading Funduscopic Images for Glaucomatous Damage," *Ophthalmology Science*, vol. 3, no. 2, Jun. 2023, doi: 10.1016/j.xops.2022.100255.

[30] S. Islam, R. C. Deo, P. D. Barua, J. Soar, and U. R. Acharya, "Novel Deep Learning Model for Glaucoma Detection Using Fusion of Fundus and Optical Coherence Tomography Images," *Sensors*, vol. 25, no. 14, Jul. 2025, doi: 10.3390/s25144337.

[31] J. N K, M. H. Ali, S. Senthil, and M. B. Srinivas, "Early detection of glaucoma: feature visualization with a deep convolutional network," *Comput Methods Biomech Biomed Eng Imaging Vis*, vol. 12, no. 1, 2024, doi: 10.1080/21681163.2024.2350508.

[32] R. Swaminathan, "An Attention Infused Deep Learning System with Grad-CAM Visualization for Early Screening of Glaucoma," May 2025, [Online]. Available: http://arxiv.org/abs/2505.17808

[33] X. Chen *et al.*, "Detecting Glaucoma in Highly Myopic Eyes From Fundus Photographs Using Deep Convolutional Neural Networks," *Clin Exp Ophthalmol*, vol. 53, no. 5, pp. 502–515, Jul. 2025, doi: 10.1111/ceo.14498.

[34] S. B. M. K., M. Kalra, and A. Zahoor, "Advancements in Deep Learning for Glaucoma Detection from Fundus Images: A Comprehensive Analysis," *Journal of Transformative Technologies and Sustainable Development*, vol. 9, no. 1, Oct. 2025, doi: 10.1007/s41314-025-00073-6.

[35] Mithunavarshini A.P and Deepa S, "A Comprehensive Survey of Deep Learning and Ensemble Techniques in Glaucoma Detection," *International Journal of Preventive Medicine and Health*, vol. 5, no. 2, pp. 9–13, Jan. 2025, doi: 10.54105/ijpmh.B1048.05020125.

[36] R. Humam Aziz and L. Abed Noor Muhammed, "Review of Glaucoma Disease Diagnosis-based Deep Learning Network," *Journal of Al-Qadisiyah for Computer Science and Mathematics*, vol. 16, no. 2, Jun. 2024, doi: 10.29304/jqcsm.2024.16.21566.

[37] W. H. Abdulsalam, R. H. Ali, S. H. Jadooa, and S. S. Hussien, "Automated Glaucoma Detection Techniques: A Literature Review," *Engineering, Technology and Applied Science Research*, vol. 15, no. 1, pp. 19891–19897, 2025, doi: 10.48084/etasr.9316.

[38] D. Mirzania, A. C. Thompson, and K. W. Muir, "Applications of deep learning in detection of glaucoma: A systematic review," Jul. 01, 2021, *SAGE Publications Ltd*. doi: 10.1177/1120672120977346.

Received: August 11, 2025 

Volume 38 No. 12s, 2025
ISSN: 1311-1728 (printed version); ISSN: 1314-8060 (on-line version)

[39] M. Hesham, G. Kareem, and M. Hadhoud, "Enhanced real-time glaucoma diagnosis: dual deep learning approach," *Bulletin of Electrical Engineering and Informatics*, vol. 14, no. 3, pp. 1846–1857, Jun. 2025, doi: 10.11591/eei.v14i3.8495.

[40] A. Aljohani and R. Y. Aburasain, "A hybrid framework for glaucoma detection through federated machine learning and deep learning models," *BMC Med Inform Decis Mak*, vol. 24, no. 1, Dec. 2024, doi: 10.1186/s12911-024-02518-y.

[41] A. Kumar and N. Katal, "A Lightweight YOLO Model for Detection of Disease from Optic Disc Region of Eye Fundus Imagery," *Sensing and Imaging 2025 26:1*, vol. 26, no. 1, pp. 45-, Apr. 2025, doi: 10.1007/S11220-025-00575-9.

[42] W. Shen and W. Zhou, "A novel Internet of Medical Things framework for absorbing bioresorbable vascular scaffold towards healthcare monitoring based on improving YOLO paradigms," *Knowl Based Syst*, vol. 322, p. 113696, Jul. 2025, doi: 10.1016/J.KNOSYS.2025.113696.

[43] S. Yin *et al.*, "Mainstream Artificial Intelligence Technologies in Contemporary Ophthalmology," *Advanced Intelligent Systems*, p. 2500055, 2025, doi: 10.1002/AISY.202500055;JOURNAL:JOURNAL:26404567;WGROUP:STRING:PUBLICATION.

[44] H. Sheraz, T. Shehryar, and Z. A. Khan, "Two stage-network: Automatic localization of Optic Disc (OD) and classification of glaucoma in fundus images using deep learning techniques," *Multimedia Tools and Applications 2024 84:14*, vol. 84, no. 14, pp. 12949–12977, Jun. 2024, doi: 10.1007/S11042-024-19338-X.

[45] X. Wang, Y. Zhang, H. Hu, and N. Wei, "Detection of retinal nerve fiber layer in patients with high myopia complicated with glaucoma by optical coherence tomography," *Technol Health Care*, vol. 33, no. 5, pp. 2425–2430, Sep. 2025, doi: 10.1177/09287329241296770;ISSUE:ISSUE:DOI.

[46] X. Wang, Y. Zhang, H. Hu, and N. Wei, "Detection of retinal nerve fiber layer in patients with high myopia complicated with glaucoma by optical coherence tomography.," *Technology & Health Care*, vol. 33, no. 5, p. 2425, Sep. 2025, doi: 10.1177/09287329241296770.

[47] A. Zhanegizov, O. Mamyrbayev, K. Momynzhanova, and N. Zhumazhan, "Effective clustering with K-means or efficient cropping with YOLO as a preprocessing step for automated fundus image standardization," *https://doi.org/10.1117/12.3077843*, vol. 13796, pp. 27–34, Sep. 2025, doi: 10.1117/12.3077843.

Received: August 11, 2025 

**Volume 38 No. 12s, 2025**

ISSN: 1311-1728 (printed version); ISSN: 1314-8060 (on-line version)

[48] R. Fang *et al.*, "Machine-Learning-Based Automated Schlemm's Canal Volumetric Segmentation for Optical Coherence Tomography," *Chemical & Biomedical Imaging*, Nov. 2025, doi: 10.1021/CBMI.5C00156.

[49] Z. Zhang *et al.*, "ORIGA(-light): an online retinal fundus image database for glaucoma analysis and research," *Annu Int Conf IEEE Eng Med Biol Soc*, vol. 2010, pp. 3065–3068, 2010, doi: 10.1109/IEMBS.2010.5626137.

[50] R. M. Masoud, R. M. A. Bakir, M. S. Saraya, and S. M. Ayyad, "BREAST-CAD: A Computer-Aided Diagnosis System for Breast Cancer Detection Using Machine Learning," *Technologies 2025, Vol. 13, Page 268*, vol. 13, no. 7, p. 268, Jun. 2025, doi: 10.3390/TECHNOLOGIES13070268.



Received: August 11, 2025